

Supporting Information

Graphene transfer method¹:

Monolayer graphene was pre-deposited on both sides of copper foil in high temperature furnace (Step 1). Poly methyl methacrylate (PMMA) (950K A3, MicroChem) was then spun on graphene sample at 4000 RPM, serving as a supporting layer (Step 2). Following this step, the other side of graphene on copper foil with no PMMA protection was removed via oxygen plasma (Step 3). The resulting PMMA-graphene-copper stack was placed floating on copper etchant (APS-100, Transene), with PMMA supporting layer facing up. After copper was completely etched, the remaining PMMA-graphene thin film stack was floating on the solution (Step 4). The thin film stack was then transferred onto the target substrate after DI water rinsing (Step 5). After baking, the PMMA supporting layer was removed with acetone bath (Step 6).

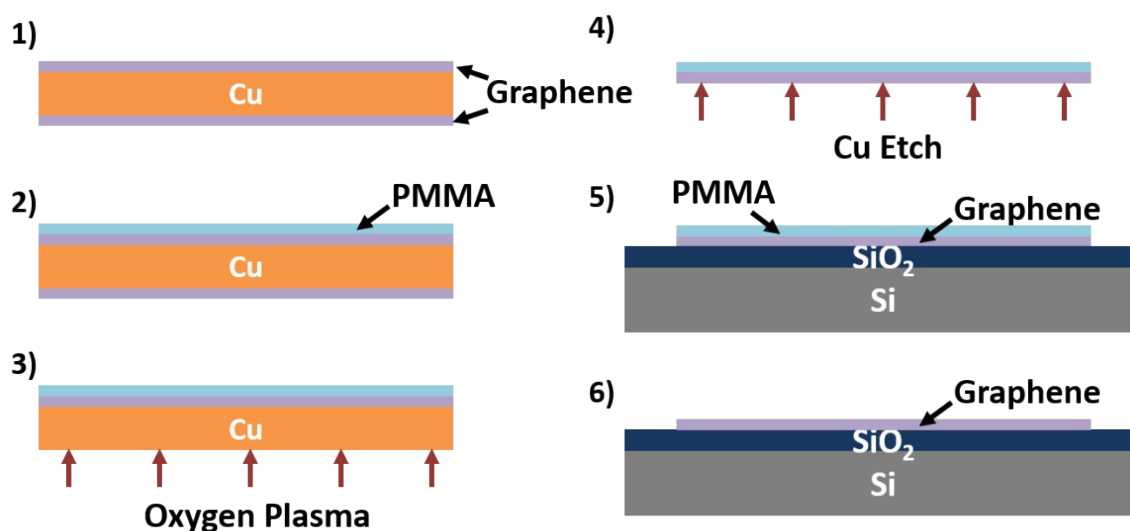


Figure S1. Graphene Transfer Process. Step (1): Chemical vapor deposition of monolayer graphene on to copper foil. Step (2): PMMA coating on graphene. Step (3): Removal of graphene on the other side with oxygen plasma. Step (4): Copper wet etch. Step (5): Transfer thin film stack (PMMA+graphene) onto target substrate. Step (6): PMMA removal.

Conformal coverage of graphene

Graphene is known to have strong adhesion with silicon dioxide substrate, especially after the wet transfer and post-baking process. This process started with scooping the PMMA-graphene thin film stack from DI water using the target substrate. Water still existed between the thin film stack and the target substrate after this step. A baking process was then employed to remove excess water between graphene and the target substrate. Baking temperature was kept below water boiling point to avoid violent vaporization process. Due to the small height to width aspect ratio of the nanochannel (~ 0.006), the thin film stack and the target substrate formed intimate contact with each other after baking due to the absence of water. The corresponding schematics describing the baking process is exhibited in Figure S2. A following baking process at higher temperature would further improve the adhesion between graphene and substrate, preventing water filling the gap between graphene and the substrate in following fabrication process.

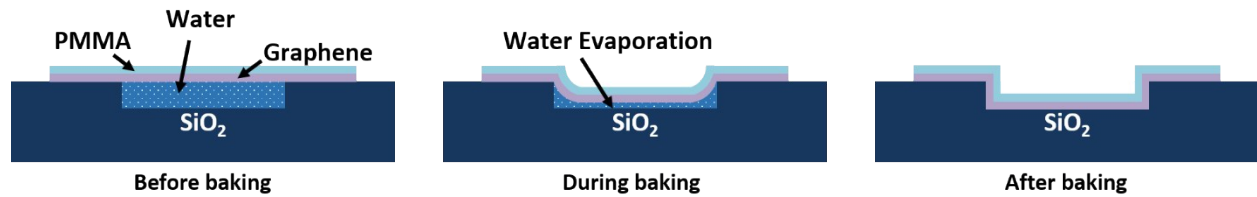


Figure S2. Schematic of baking process. a) Water existence between PMMA-graphene stack and surface structures right after wet transfer process. b) Water trapped in surface structures started to evaporate during baking process. Distance between thin film stack and substrate became closer at the same time. c) Water was completely removed and graphene conformally covered the surface structures due to small aspect ratio.

Figure S3 shows the surface profile of an open graphene nanochannel scanned by atomic force microscope (AFM). The graphene coated surface has almost the same roughness as the original silica surface, which is around 0.3 nm and thus both can be considered as atomically smooth surfaces.

The depth of open graphene nanochannel (~20 nm) is almost the same as the depth of silica channel before graphene transfer, demonstrating the conformal coating of graphene on the silica channel surface.

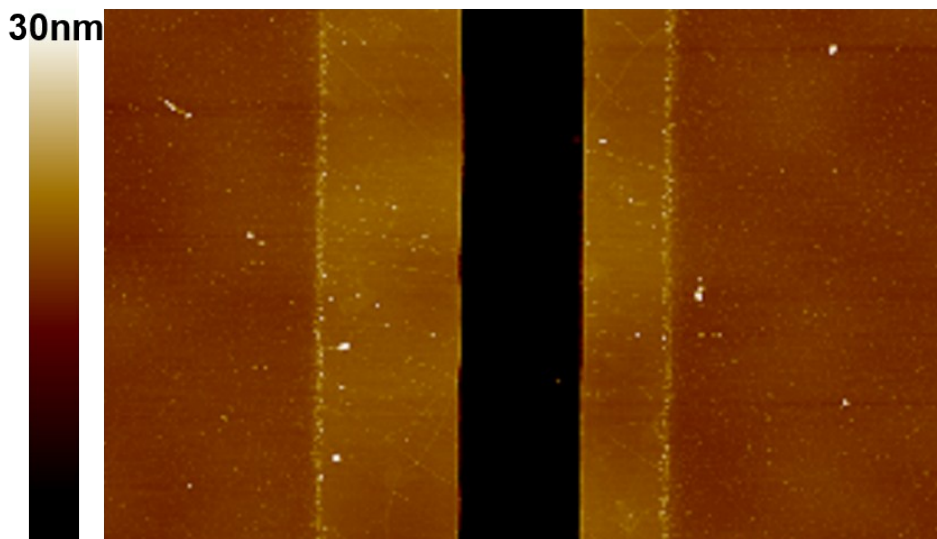


Figure S3. AFM profile of open graphene nanochannel.

Figure S4 shows the surface height profiles for open nanochannels before and after graphene wet transfer. According to the surface height profile, the silica channel (red line) and graphene channel (blue line) have the same height (~20nm) and thus confirm the conformal coverage of graphene on the nanochannels. The AFM scanned step height of graphene adhere to SiO₂ surface is roughly 2-3 nm, which deviates from reported monolayer graphene thickness (~0.4 nm). This discrepancy can be explained by instrument offset due to tip-substrate interaction.^{2, 3}

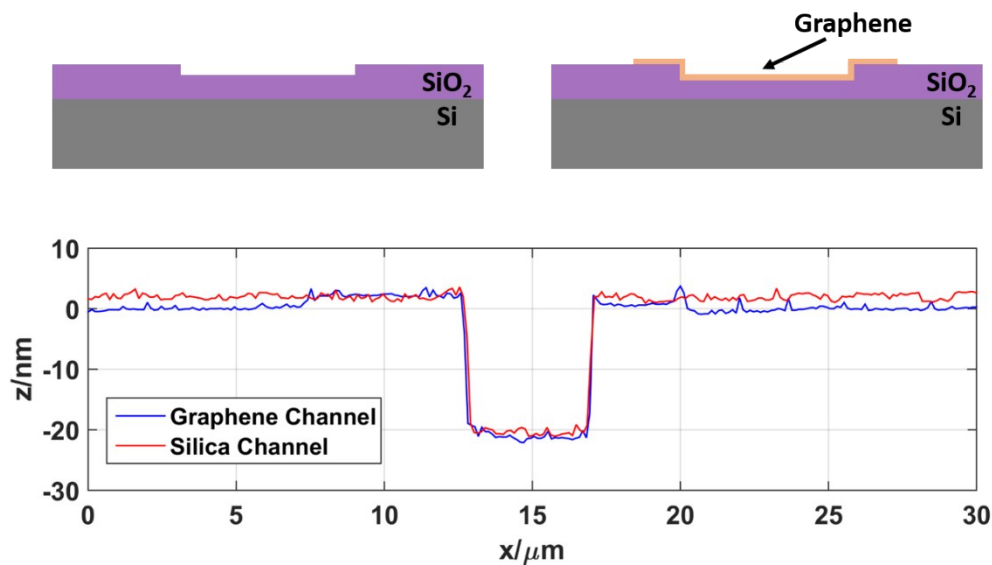


Figure S4. Surface profile of nanochannel before and after graphene transferring process.

Anodic bonding under vacuum environment

The silicon chip (with graphene nanochannel) and the glass chip (with microchannels and reservoirs) were cleaned with acetone, isopropanol and deionized water and brought together right afterwards to form intimate contact with each other. As shown in Figure S4, the resulting chip stack was then sandwiched between a copper cap and copper block inside our home-made vacuum chamber. Four ceramic screws were used to fix the copper cap and apply normal force onto the chip stack. In addition, the electrically insulated ceramic screws can ensure most bonding current passed through the chip stack.

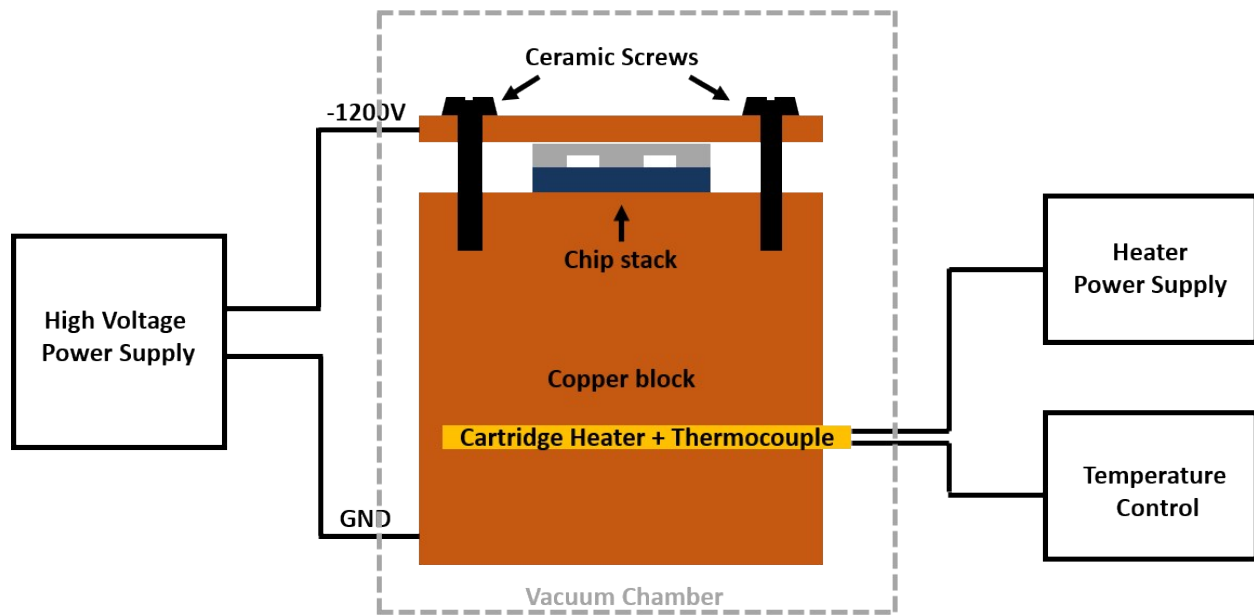


Figure S5. Schematic of the anodic bonding setup under vacuum environment.

After electric and thermal connection was made, chips were heated to 450°C with a cartridge heater embedded in the copper block. 800V voltage was applied to the chip stack to form permanent bond after temperature was stable within 0.5°C. The bonding current as a function of time is shown in Figure S5.

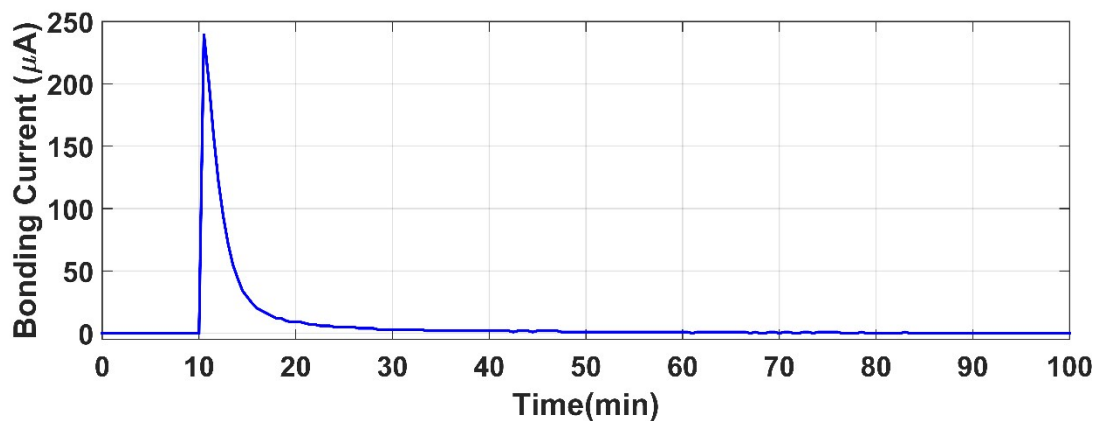


Figure S6. Typical bonding current over time.

PNP Model Description

Poisson-Nernst-Planck modeling system has been widely used to explain the ion transport through nanoscale conduits. Specifically, the Poisson equation describes the distribution of electrical potential while the Nernst-Planck equation describes the motion of ions under the influence of concentration gradient and electric field. The governing equation of the PNP model are listed here:

Poisson Equation:

$$\nabla^2 \psi = - \frac{\rho_e}{\epsilon \epsilon_0}$$

Nernst-Planck Equation:

$$\nabla \cdot J_i = 0$$

$$J_i = - D_i \nabla c_i - \frac{D_i z_i e}{k_B T} c_i \nabla \psi$$

Nomenclature:

ψ	local electric potential
ρ_e	local net charge density
ϵ	dielectric constant of water
ϵ_0	permittivity of free space
J_i	ion flux of species i
D_i	diffusivity of species i
c_i	local ion concentration of species i
e	basic charge
z_i	valence of ion i
k_B	Boltzmann constant
T	temperature
σ	surface charge density

A 2-D domain was built to model the ion transport inside our nanochannel. The total channel length in our model is 1 μm and the channel height is 20 nm. In this model, by assuming the surface charge density of the floor and the ceiling of the nanochannel, we first solved the distributions of electrical potential and ion concentrations along the channel height direction. Electrophoretic and electroosmotic conductance of the real nanochannel at this certain surface charge density were then calculated by assuming the same potential and ionic concentration distribution across the channel height.

Electrochemical conductance contribution analysis

To understand the electrochemical contribution in measured conductance of Type II devices, we compare the measured KCl conductance with NaCl conductance in the exact same device. Since the possibly involved electrochemical reaction^{4, 5} does not involve K^+ , Na^+ and Cl^- , electron transfer rate at graphene/solution interface of the exact device should be the same for KCl and NaCl solutions at same concentration. Accordingly, the conductance from electrochemical reaction should also be the same for both solutions at the same concentration. We assume this electrochemical conductance is $G(n)$, as it could only be the function of ionic concentration, n . The conductance solely coming from electrokinetic flow inside graphene nanochannels is defined as $G_K(n)$ and $G_{Na}(n)$ representing those with KCl and NaCl solutions, respectively. The total conductance for graphene channel devices thus can be viewed as the sum of electrochemical conductance and electrokinetic conductance. Here the total conductance ratio of KCl and NaCl

solutions, $\tau = \frac{G_K(n) + G(n)}{G_{Na}(n) + G(n)}$, serves as an important indicator for the contribution of electrochemical conductance $G(n)$. If τ is independent of n and always close to 1, $G(n)$ is more

dominant in the entire system. In contrast, if $\tau \sim \tau_{EKF} = \frac{G_K(n)}{G_{Na}(n)}$, $G(n)$ becomes negligible compared with the electrokinetic conductance.

We use our Poisson-Nernst-Planck (PNP) model to calculate $G_K(n)$ and $G_{Na}(n)$ for KCl and NaCl solutions from 10^{-6} M to 1 M and then calculate the theoretical conductance ratio solely from electrokinetic flow, τ_{EKF} . Our model assumes that there are 4 major ions in KCl (NaCl) solution, including K^+ (Na^+), Cl^- , H^+ and OH^- . H^+ concentrations are further assumed to be equal to 10^{-6} M due to CO_2 adsorption and dissociation during the actual experiments. The simulation curve (dashed line) is displayed in Figure S7 as a reference. At very low concentrations (e.g. 1 μ M), surface charge governs the ion concentration inside nanochannel. Consequently, only cations would contribute to the electrokinetic conductance due to negative surface charges and overlapped electrical double layers. The contributing cations include both K^+ and H^+ because the proton concentration is comparable to major cations K^+/Na^+ concentration. Since proton mobility ($36.27 \times 10^{-8} \text{ m}^2\text{V}^{-1}\text{s}^{-1}$) is much higher than mobilities of K^+ ($7.6 \times 10^{-8} \text{ m}^2\text{V}^{-1}\text{s}^{-1}$) and Na^+ ($5.19 \times 10^{-8} \text{ m}^2\text{V}^{-1}\text{s}^{-1}$), the electrokinetic conductance at such low concentrations would actually mainly be determined by the proton transport inside the nanochannels, and the conductance ratio τ_{EKF} is close to 1 at 1 μ M. As the bulk concentration increases (from 10^{-6} M to 10^{-4} M), while ion concentrations in the nanochannels are still governed by surface charge, contribution from protons becomes less significant due to their relative low concentration compared to K^+ (Na^+), and the conductance ratio τ_{EKF} becomes more dominated by the electrophoresis of K^+ and Na^+ inside channel. Therefore, τ_{EKF} should increase with the increasing bulk concentration and become more and more close to the mobility ratio of K^+ to Na^+ ($\mu_{K^+}/\mu_{Na^+} = 1.46$). Our

simulation shows the conductance ratio τ_{EKF} reaches the maximum value ($\tau_{EKF} = 1.35$) at the concentration of 0.1 mM. This maximum value is slightly smaller than the mobility ratio of K^+ to Na^+ , which can be explained by the presence of electroosmotic flow since its contribution to the total ionic conductance does not depend on the type of monovalent cations in solution. As the bulk concentration continues increasing, electric double layers are no longer overlapping inside nanochannels. Electrophoretic flow contributed by anions (Cl^-) cannot be ignored because its concentration becomes comparable to cations (K^+ , Na^+) inside nanochannel. The conductance ratio thus decreases as the increasing bulk concentration and finally becomes close to the

mobility ratio of the sum of cations and anions, $\frac{\mu_{K^+} + \mu_{Cl^-}}{\mu_{Na^+} + \mu_{Cl^-}} = 1.18$, as the bulk concentration approaches 1 M.

The conductance ratio of KCl and NaCl solutions is calculated based on conductance measurement result of the same device. To avoid time variation and contamination issue, measurements for twin solutions at all concentrations were carried out consecutively within 10 hours. Three Type II devices (graphene channel) and one Type I devices (silica channel) were tested and results are also exhibited in Figure S7. The experimental data collected from both Type I and II devices agree with our simulation curve where only the electrokinetic flow is considered, exhibiting an increasing and decreasing trend with monotonously increasing bulk concentration. This result convinces us that the measured conductance in Type II devices can reflect the electrokinetic conductance inside the graphene nanochannels to a large extent. Consequently, the higher conductance measured in Type II devices for KCl solutions mainly comes from the enhancement of electrokinetic flow in the graphene nanochannels.

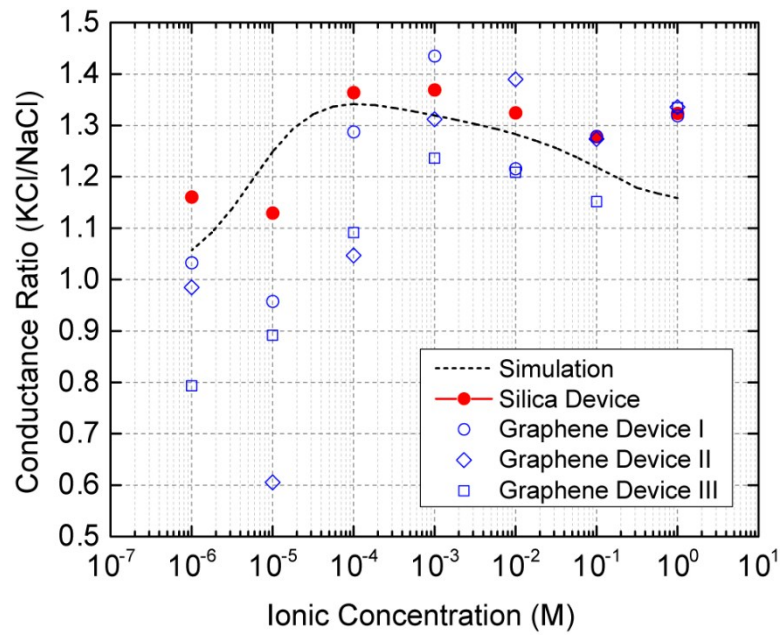


Figure S7 Experimental and theoretical ionic conductance ratio (KCl/NaCl) for Type I (silica) and Type II (graphene) devices. All the devices tested have the exact same geometry.

Reference

1. Li, X.; Zhu, Y.; Cai, W.; Borysiak, M.; Han, B.; Chen, D.; Piner, R. D.; Colombo, L.; Ruoff, R. S., Transfer of Large-Area Graphene Films for High-Performance Transparent Conductive Electrodes. *Nano Letters* **2009**, *9* (12), 4359-4363.
2. Novoselov, K. S.; Geim, A. K.; Morozov, S. V.; Jiang, D.; Zhang, Y.; Dubonos, S. V.; Grigorieva, I. V.; Firsov, A. A., Electric Field Effect in Atomically Thin Carbon Films. *Science* **2004**, *306* (5696), 666-669.
3. Nemes-Incze, P.; Osváth, Z.; Kamarás, K.; Biró, L. P., Anomalies in thickness measurements of graphene and few layer graphite crystals by tapping mode atomic force microscopy. *Carbon* **2008**, *46* (11), 1435-1442.
4. Chakrapani, V.; Angus, J. C.; Anderson, A. B.; Wolter, S. D.; Stoner, B. R.; Sumanasekera, G. U., Charge Transfer Equilibria Between Diamond and an Aqueous Oxygen Electrochemical Redox Couple. *Science* **2007**, *318* (5855), 1424-1430.
5. Levesque, P. L.; Sabri, S. S.; Aguirre, C. M.; Guillemette, J.; Sij, M.; Desjardins, P.; Szkopek, T.; Martel, R., Probing charge transfer at surfaces using graphene transistors. *Nano Lett* **2011**, *11* (1), 132-7.